nature ecology & evolution

Article

https://doi.org/10.1038/s41559-023-02255-x

Drug dependence in cancer is exploitable by optimally constructed treatment holidays

Received: 6 July 2022

Accepted: 19 October 2023

Jeff Maltas [1,5], **Shane T. Killarney** [2,5], **Katherine R. Singleton**[2,5], **Maximilian A. R. Strobl** [3], **Rachel Washart**[2], **Kris C. Wood** [2] & **Kevin B. Wood** [1,4]

Cancers with acquired resistance to targeted therapy can become simultaneously dependent on the presence of the targeted therapy drug for survival, suggesting that intermittent therapy may slow resistance. However, relatively little is known about which tumours are likely to become dependent and how to schedule intermittent therapy optimally. Here we characterized drug dependence across a panel of over 75 MAPK-inhibitor-resistant *BRAF*$^{\mathrm{V600E}}$ mutant melanoma models at the population and single-clone levels. Melanocytic differentiated models exhibited a much greater tendency to give rise to drug-dependent progeny than their dedifferentiated counterparts. Mechanistically, acquired loss of microphthalmia-associated transcription factor in differentiated melanoma models drives ERK–JunB–p21 signalling to enforce drug dependence. We identified the optimal scheduling of 'drug holidays' using simple mathematical models that we validated across short and long timescales. Without detailed knowledge of tumour characteristics, we found that a simple adaptive therapy protocol can produce near-optimal outcomes using only measurements of total population size. Finally, a spatial agent-based model showed that optimal schedules derived from exponentially growing cells in culture remain nearly optimal in the context of tumour cell turnover and limited environmental carrying capacity. These findings may guide the implementation of improved evolution-inspired treatment strategies for drug-dependent cancers.

In unresectable or metastatic *BRAF*$^{\mathrm{V600E}}$ melanoma, patients are commonly treated in the first line with a combination of CTLA-4 and PD-1 immunotherapy, yielding 5 year survival rates over 50% (ref. 1). Patients who fail to respond or develop resistance to immunotherapy, or cannot remain on therapy because of toxicity, commonly switch to MAPK inhibitor (MAPKi) therapy targeting BRAF plus MEK, further improving clinical outcomes[2,3]. Unfortunately, the eventual emergence of resistance to MAPKi is a common outcome in these patients[4]. Interestingly, numerous reports have revealed that upon resistance to targeted BRAF-plus-MEK inhibitors, *BRAF*$^{\mathrm{V600E}}$ mutant melanomas may become dependent on these inhibitors for survival[5–9]. Mechanistically, it was found that withdrawing MAPKi treatment in resistant tumours hyperactivates ERK1/2 through derepressed BRAF activity combined with the intrinsic and adaptive resistance mechanisms used to survive treatment[8]. Overstimulation of ERK2 induces the AP-1 transcription factors JunB and FRA1, which were discovered to drive p21-dependent

---

[1]Department of Biophysics, University of Michigan, Ann Arbor, MI, USA. [2]Department of Pharmacology and Cancer Biology, Duke University, Durham, NC, USA. [3]Department of Translational Hematology and Oncology Research, Cleveland Clinic, Cleveland, OH, USA. [4]Department of Physics, University of Michigan, Ann Arbor, MI, USA. [5]These authors contributed equally: Jeff Maltas, Shane T. Killarney, Katherine R. Singleton. e-mail: kris.wood@duke.edu; kbwood@umich.edu

cell cycle arrest following MAPKi withdrawal in drug-dependent models[7,9]. These pioneering preclinical studies suggest that incorporating 'drug holidays' might effectively slow disease progression in patients who are MAPKi resistant. A large-scale phase 2 clinical trial compared continuous with intermittent BRAF-plus-MEK inhibition for patients with *BRAF*^{V600E} melanoma to further test this idea. Disappointingly, in this trial, intermittent dosing did not improve the primary end-point of progression-free survival in patients compared with continuous therapy[10].

One potential explanation for the discrepancy between preclinical and clinical outcomes for intermittent therapy is our incomplete understanding of the factors contributing to the drug dependence phenotype. As a result, it is currently impossible to select patients whose tumours are most likely to develop drug dependence and are most likely to respond to intermittent therapy. *BRAF*^{V600E} mutant melanomas exhibit substantial phenotypic heterogeneity[11]. These tumours are transcriptionally classified across a continuous spectrum of differentiation states, which include melanocytic, transitory, neural crest like and undifferentiated[12]. A unique transcriptional signature defines each differentiation state but can be identified via relative levels of governing transcription factors (microphthalmia-associated transcription factor (MITF), SOX10 and SOX9) and receptor tyrosine kinases (AXL, NGFR and epidermal growth factor receptor (EGFR)). Differentiated melanoma is considered more proliferative and is defined by MITF^{high}, SOX10^{high}, AXL^{low} and EGFR^{low}. Undifferentiated melanoma has a transcriptional signature resembling epithelial-to-mesenchymal transition, is thought to be more invasive and is defined by being MITF^{low}, SOX10^{low}, AXL^{high} and EGFR^{high}. Although melanoma differentiation states are known to alter phenotypic responses to both immunotherapy[13–15] and targeted therapy[16–18], it is poorly understood whether they contribute to drug dependence.

A second potential explanation for the clinical failure of intermittent therapy in patients with *BRAF*^{V600E} mutant melanoma is the possibility that the intermittent dosing schedule used in the trial was suboptimal. This intermittent dosing schedule was adapted from studies performed in a preclinical immunodeficient mouse model with single-agent BRAF inhibition rather than the BRAF-plus-MEK inhibition used in the trial[5,10]. It is possible that an alternative scheduling approach may have worked better, although it is uncertain how such an approach would be designed.

Recently, there has been a movement towards evolution-informed therapies[19–21]. These therapies aim to treat cancers (and other diseases) as heterogeneous, ecologically diverse, evolving populations[22]. For example, recent laboratory work in cancer and bacteria aims to take advantage of drug sensitivities that evolve due to the initial treatment, a phenomenon known as 'collateral sensitivity'[23–26]. More ecologically inspired therapies take advantage of the competition for resources between distinct clonal populations, hypothesizing that more treatable clones may win out in a competition for shared resources[27,28]. Evolutionary game theory has also been leveraged to quantify and exploit distinct interactions between clonal populations[29–31]. Still, much of the existing literature on evolution-based therapies is theoretical. It is unclear how an evolution-inspired therapy might optimally treat a cancer cell population that includes drug-dependent cells.

In this Article, we take an essential step towards understanding the frequency of drug dependence in *BRAF*^{V600E} mutant melanoma, the factors that determine a tumour's propensity to acquire drug dependence and how intermittent therapeutic strategies may be optimally administered to mixed cancer cell populations to minimize population growth over time.

Results

Melanoma differentiation state correlates with drug dependence

We began investigating drug dependence by deriving resistance to single-agent or combination BRAF (PLX4720) and MEK (AZD6244) inhibition across *BRAF*^{V600E} mutant melanoma cell lines (Supplementary Fig. 1a). We chose A375, HS294T, WM793, SKMEL5 and SKMEL28 *BRAF*^{V600E} mutant models as they are well characterized in the literature[32,33] and the Cancer Dependency Map Project (DepMap)[34]. We maintained a pooled population of each resistant model to preserve phenotypic diversity. Once the resistant populations began proliferating through high-dose MAPKi, we assessed their dependence on the treatment (Fig. 1a–c). We defined drug dependence as the ability of MAPKi-resistant cells to proliferate at least twice as rapidly in the presence of MAPKi than without it. We found mixed evidence of drug dependence across MAPKi-resistant cell lines at the population level. Whereas the SKMEL5 and SKMEL28 cell lines exhibited a strong drug dependence phenotype (Fig. 1a–c), the A375, HS294T and WM793 cell lines did not (Fig. 1a–c).

Next, we sought to understand why specific *BRAF*^{V600E} mutant models gave rise to drug dependence. Initial experiments were performed with 12 pooled populations of resistant clones, and we hypothesized that drug-dependent cell lines were selected for a unique drug resistance mechanism that dominated the pooled population and gave rise to drug dependence. To investigate this question, we quantified drug dependence across over 65 individual MAPKi-resistant clones in A375, UACC62, COLO679, SKMEL5 and SKMEL28 *BRAF*^{V600E} mutant cell lines (Fig. 1d). We found no emergence of drug-dependent clones in either A375 or UACC62 cell lines despite the fact that A375 cells are known to give rise to a multitude of resistance mechanisms[35] (Fig. 1d). Interestingly, we found that almost all resistant clones from the COLO679, SKMEL5 and SKMEL28 cell lines became MAPKi dependent upon resistance (Fig. 1d). These data suggest that no specific resistance mechanism is associated with drug dependence, a point observed by others[9], and that, rather, a difference in the baseline characteristics of the cell lines may contribute to the emergence of MAPKi dependence.

Next, we compared the drug-naive gene expression profiles of cell lines that give rise to resistant–dependent progeny (COLO679,

Fig. 1 | Melanocytic melanoma is primed for addiction to MAPK inhibition upon resistance. a, Parental and PLX4720-resistant melanoma cell lines were seeded at a concentration of 1,000 cells per ml and treated every 72 h with DMSO or 3 μM PLX4720 (BRAFi). **b**, Parental and AZD6244-resistant melanoma cell lines were seeded at a concentration of 1,000 cells per ml and treated every 72 h with DMSO or 3 μM AZD6244 (MEKi). **c**, Parental and PLX4720-plus-AZD6244-resistant melanoma cell lines were seeded at a concentration of 1,000 cells per ml and treated every 72 h with DMSO or 3 μM PLX4270 plus 3 μM AZD6244. For **a**–**c**, crystal violet staining was performed when the DMSO-treated parental group reached confluency. Drug-dependent conditions are shown in red. **d**, Individual PLX4720-resistant clones from the specified cell lines were subjected to identical experimental conditions as in **a**. Drug-dependent clones are shown in red. Data are representative of the following number of biologically independent samples: A375, $n = 9$; UACC62, $n = 19$; COLO679, $n = 8$; SKMEL5, $n = 12$; and SKMEL28, $n = 19$. **e**, Two-class comparison of the DepMap Expression (Public 22Q4) dataset between 'in-group' addictive (COLO679, SKMEL5 and SKMEL28) and 'out-group' non-addictive (WM793, A375 and HS294T) cell lines. The top 100 DEGs involved in melanoma differentiation states are shown in the indicated colour. Refer to Methods for detailed statistical information. **f**, GSEA results from the ranked gene list from **e**. Enrichment plot of the melanocytic differentiation gene set and associated normalized enrichment score (ES) (top panel). Normalized ESs of melanoma differentiation gene sets (bottom panel). **g**, DepMap Expression (Public 22Q4) comparison between addictive (COLO679, SKMEL5 and SKMEL28 ($n = 3$)) and non-addictive (WM793, A375 and HS294T ($n = 3$)) cell lines of the specified genes represented in transcripts per million (TPM). **h**, Western blot of the indicated proteins in the parental melanoma cell lines. In **a**–**c** and **h**, the data are representative of three biologically independent experiments ($n = 3$). In **a** and **g**, data are presented as mean ± s.e.m.

SKMEL5 and SKMEL28) with those of cell lines that give rise to resistant–non-dependent progeny (A375, HS294T and WM793) in DepMap. Strikingly, the top 100 differentially expressed genes (DEGs) between the former and latter groups were enriched in processes related to melanoma differentiation (Fig. 1e). Using melanoma differentiation gene sets previously identified[12], we found that cell lines that give rise to drug-resistant dependent progeny are enriched in the melanocytic gene expression signature (Fig. 1f). We confirmed that these cell lines were more differentiated at baseline, as defined by their increased expression of MITF, SOX10, MLANA and PMEL and their decreased

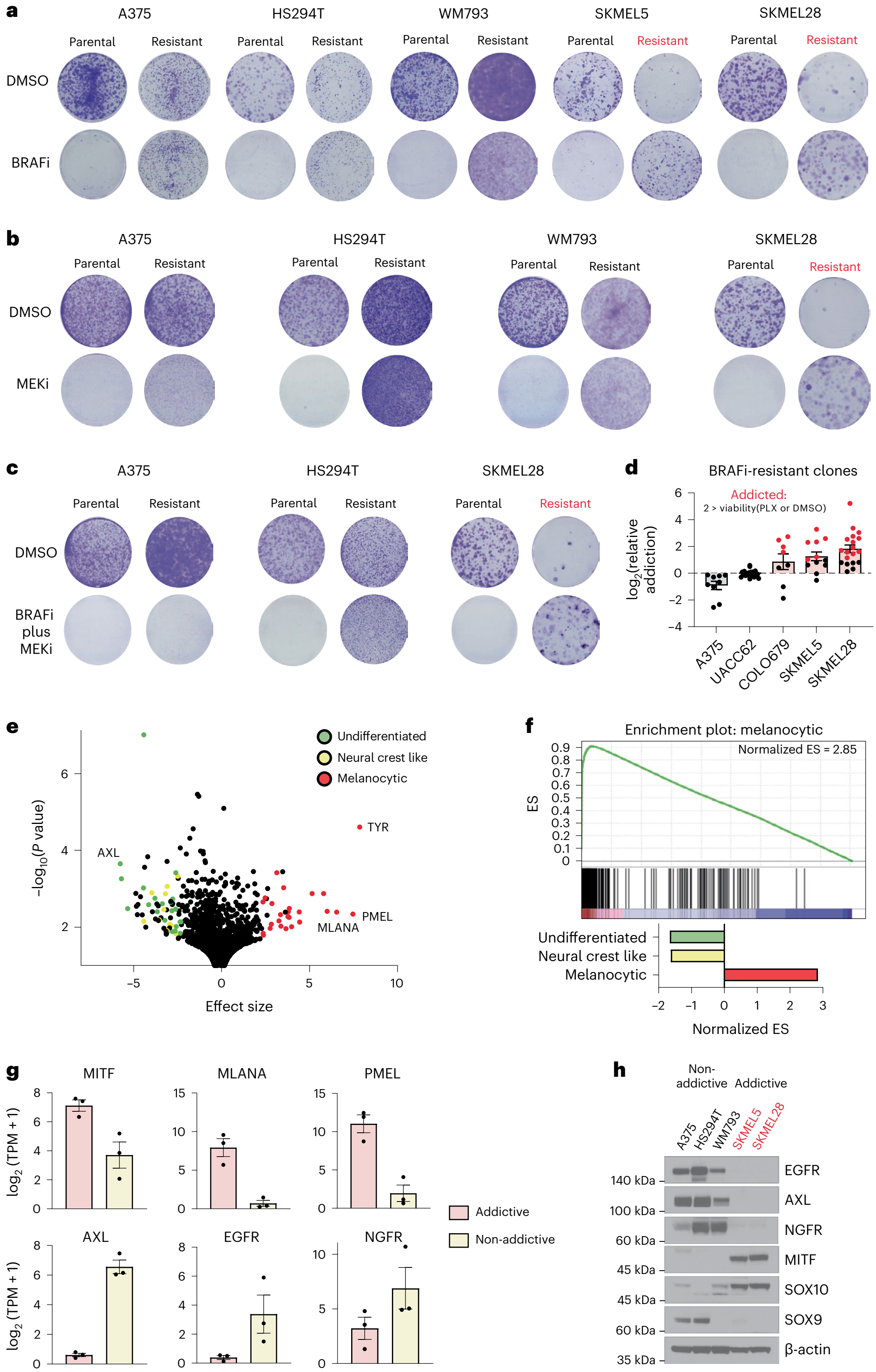

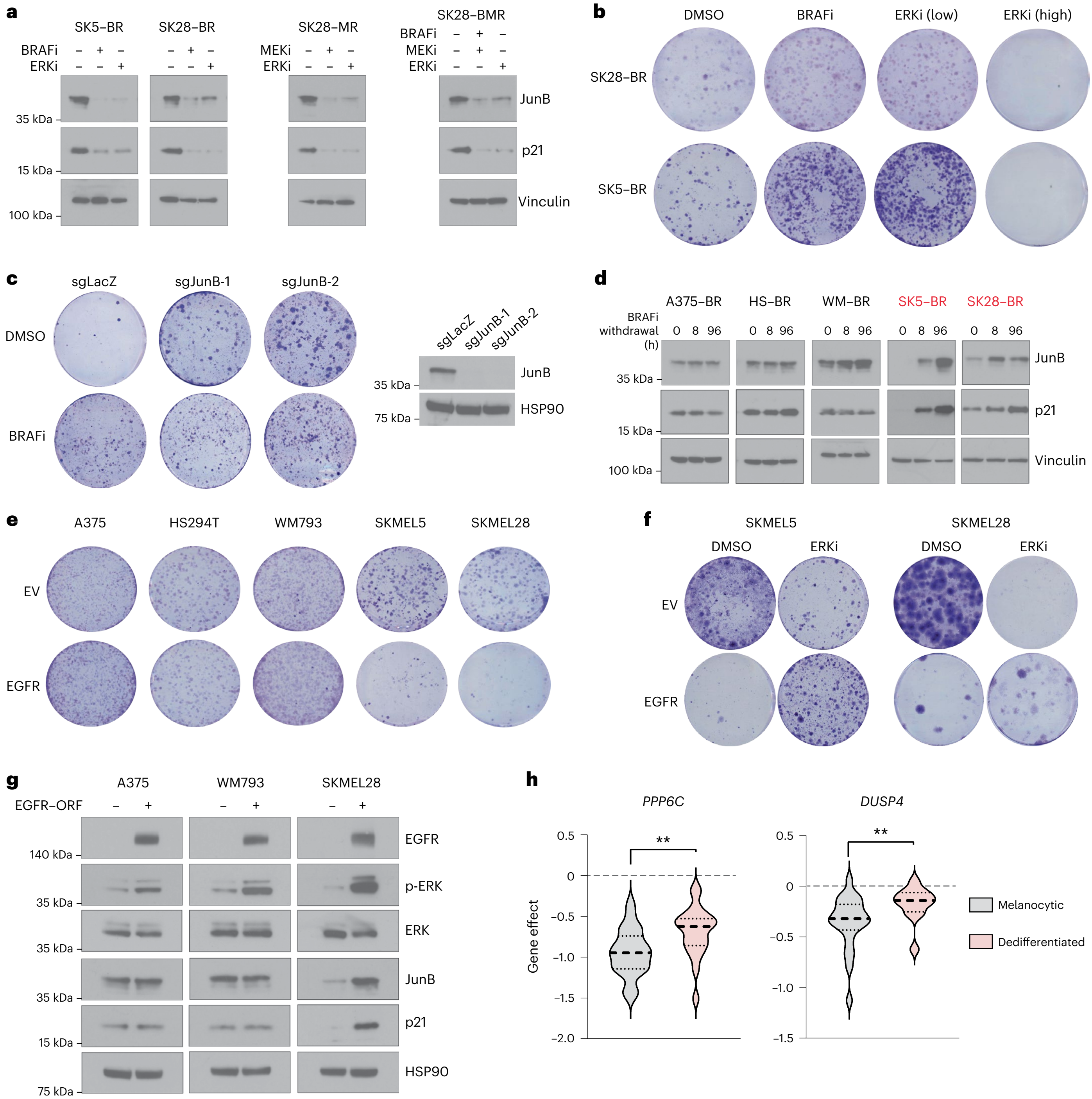

Fig. 2 | Dedifferentiated melanoma is resistant to ERK-induced cell cycle arrest. a, Western blot of indicated proteins in cell lines that were SKMEL5–BR (SK5–BR), SKMEL28–BR (SK28–BR), SKMEL28–MR (SK28–MR) and SKMEL28–BMR (SK28–BMR), treated with the specified doses of DMSO, 3 μM PLX4720 (BRAFi), 3 μM AZD6244 (MEKi) or 50 nM SCH772984 (ERKi) for 96 h. **b**, SK28–BR and SK5–BR cells were treated every 72 h with the indicated drug. Crystal violet staining was performed when each cell line reached confluency. **c**, Left, SK5–BR cells with two sgRNAs targeting JunB and one non-targeting control were treated with DMSO or 3 μM PLX4720 every 72 h. Crystal violet staining was performed on day 14 following seeding. Right, western blot validation of JunB knockout. **d**, Western blot analysis of indicated proteins in BRAFi-resistant A375 (A375–BR), HS294T (HS–BR), WM793 (WM–BR), SK5–BR and SK28–BR cell lines following BRAFi withdrawal for the specified time. Drug-dependent models are shown in red. **e**, Melanoma cell lines with empty vector (EV) or EGFR–ORF construct were seeded in media that contained 2.5 ng ml^{-1} of EGF. Crystal violet staining was performed when each cell line's EV condition reached confluency. **f**, SKMEL5 and SKMEL28 EV- and EGFR–ORF-transduced cell lines treated with DMSO or 50 nM SCH772984 (ERKi), refreshed every 72 h. Cells were seeded in media containing 2.5 ng ml^{-1} of EGF. **g**, Western blot analysis of melanoma cell lines transduced with EV or EGFR–ORF following 96 h of treatment with 5 ng ml^{-1} EGF. **h**, Left, analysis of *PPP6C* DepMap CRISPR gene score across melanocytic ($n = 26$) and dedifferentiated ($n = 21$) MAPK-mutant melanoma. Right, analysis of *DUSP4* and gene effect across melanocytic ($n = 23$) and dedifferentiated ($n = 12$) MAPK-mutant melanoma using the DepMap RNAi (Achilles plus DRIVE plus Marcotte, DEMETER2) dataset. Two-tailed unpaired *t*-test, $^{**}P < 0.01$. In **a**–**g**, the data represent three independent experiments ($n = 3$).

expression of EGFR, NGFR, AXL and SOX9 (Fig. 1g,h). Reciprocally, we found that cell lines that give rise to MAPKi-resistant non-dependent progeny exhibited neural-crest-like and undifferentiated characteristics, as defined by their inverse expression of these markers (Fig. 1g,h). Together, these data suggest that the drug-naive differentiation state of melanoma is tightly correlated with the ability to become MAPKi dependent upon resistance.

Dedifferentiated melanoma is resistant to ERK-induced cell cycle arrest

Drug dependence in *BRAF*^{V600E} melanoma is driven by the ERK2–JunB/FRA1–p21 signalling axis[6,7,9]. Specifically, removing MAPKi from drug-dependent cell lines hyperactivates ERK2, inhibiting cell cycle progression through JunB/FRA1-dependent accumulation of p21. We therefore hypothesized that the melanoma cell differentiation state modulates ERK2–JunB/FRA1–p21 signalling. To investigate this, we first validated that the drug-dependent, melanocytic, MAPKi-resistant SKMEL5 and SKMEL28 models induce JunB–p21 in an ERK-dependent manner following the withdrawal of the drug (Fig. 2a). We found p21 accumulation in the drug-dependent models to be associated with a significant accumulation of cells in the G1 phase (Supplementary Fig. 1b) and an increase in β-galactosidase (β-gal) staining (Supplementary Fig. 1c). p21-dependent cell cycle arrest was reversed by low-dose ERK inhibitor (SCH772984) treatment, which rescued cell proliferation to levels equal to that observed in the context of BRAF inhibitor (BRAFi) treatment (Fig. 2a,b). In addition, we confirmed that knockout of JunB with CRISPR/Cas9 rescued cell proliferation upon drug removal (Fig. 2c). Interestingly, we did not observe clear evidence of increased phosphorylation of FRA1 following drug removal in drug-dependent models relative to drug-non-dependent models (Supplementary Fig. 1d). Together these data confirm previous reports showing that the ERK–JunB–p21 pathway drives cell cycle arrest in drug-dependent models[7,9].

The non-dependent and dedifferentiated A375, HS294T and WM793 resistant models did not induce JunB–p21 signalling (Fig. 2d), G1 arrest (Supplementary Fig. 1b) or β-gal staining (Supplementary Fig. 1c) following MAPKi withdrawal. Furthermore, A375, HS294T and WM793 MAPKi-resistant models showed phospho-ERK rebound upon drug withdrawal and remained sensitive to SCH772984, suggesting that resistance in these models is indeed driven by ERK reactivation (Supplementary Fig. 1e,f) rather than an ERK-independent mechanism[36]. We next tested whether dedifferentiated melanoma models were resistant to direct activation of ERK–JunB–p21 signalling. To activate ERK, wild-type EGFR was ectopically expressed in A375, HS294T, WM793, SKMEL5 and SKMEL28 parental cell lines, and growth kinetics were measured. Compared with matched controls, melanocytic melanoma cell growth (SKMEL5 and SKMEL28) was potently inhibited following EGFR expression (Fig. 2e). Interestingly, EGFR expression did not affect proliferation in dedifferentiated melanoma models (A375, HS294T and WM793s; Fig. 2e). The sensitivity to EGFR expression and activation of JunB–p21 in the melanocytic cell lines was rescued by low-dose SCH772984 treatment, confirming ERK-hyperactivation-dependent growth inhibition (Fig. 2f and Supplementary Fig. 2a). Furthermore, hyperactivation of ERK via EGFR expression induced JunB–p21 in melanocytic but not dedifferentiated cells (Fig. 2g). Collectively, these data indicate that dedifferentiated melanoma models are resistant to JunB–p21-dependent cell cycle arrest following ERK hyperactivation.

To further understand the impact of differentiation state on sensitivity to ERK–JunB–p21 hyperactivation, we performed single-sample gene set enrichment analysis (ssGSEA) on every *BRAF*- and *NRAS*-mutant melanoma cell line annotated in DepMap. Based on their transcriptomic profile, we classified lines as ‘melanocytic’ or ‘dedifferentiated’. We included neural-crest-like and undifferentiated differentiation states into the ‘dedifferentiated’ grouping. Interestingly, dedifferentiated melanoma was significantly more resistant to loss of dual specificity phosphatase 4 (*DUSP4*) and protein phosphatase 6 catalytic subunit (*PPP6C*) when compared to melanocytic melanoma (Fig. 2h). DUSP4 and PPP6C are phosphatases that negatively regulate ERK signalling in MAPK-mutant melanoma. Genetic silencing of either gene leads to hyperactivation of ERK[37–39], which suggests that across a broad panel of models, melanocytic differentiated melanomas are sensitive to ERK hyperactivation while dedifferentiated melanomas are relatively resistant.

Manipulation of differentiation state modulates MAPKi dependence

Next, we sought to investigate the mechanistic basis for the observed correlation between melanoma differentiation state and drug dependence. Melanocytic melanoma is defined by its expression of MITF and SOX10. Interestingly, it is known that acquired resistance to MAPKi can occur through dedifferentiation via the loss of MITF[16,40]. Consistent with this concept, SKMEL28 cells dedifferentiated into a MITF^{low}, SOX10^{low}, EGFR^{high} and AXL^{high} state upon MAPKi resistance (Fig. 3a), which has been previously characterized in this model[16]. We measured cell surface EGFR levels in the parental and BRAFi-resistant SKMEL28 cells and found no evidence of EGFR^{high} clones in the parental population (Supplementary Fig. 2b), suggesting that the evolution of resistance in this case may not involve selection for an intrinsically resistant, EGFR^{high} clone, but rather an adaptive dedifferentiation process, consistent with previous work[41–43].

As MAPKi forces dedifferentiation in the SKMEL28 model, it was surprising that these cells were drug dependent and sensitive to ERK–JunB–p21 signalling. We hypothesized the MAPKi-resistant SKMEL28 cells retained molecular features of the melanocytic parental state, which would explain their continued sensitivity to ERK hyperactivation. We first assessed JunB and FRA1 protein levels across all DepMap melanoma cell lines and observed a significant increase in levels of JunB, but not FRA1, protein in dedifferentiated melanoma compared with melanocytic melanoma cell lines (Fig. 3b and Supplementary Fig. 2c,d). To understand whether this increase in protein expression was correlated with JunB transcriptional activity, we created a JunB transcriptional signature by taking the top 100 upregulated genes from a recent JunB overexpression experiment in A375 melanoma cells[44]. We performed ssGSEA with the JunB target gene signature on ~1,400 available cell lines in DepMap to give each cell line a JunB target score and found a significant positive correlation between JunB mRNA with the JunB target gene score across all cell lines (Supplementary Fig. 2e), which suggests the target gene signature appropriately represents JunB transcriptional activity. We then identified that dedifferentiated melanoma has a transcriptional profile significantly enriched for JunB target genes compared with melanocytic melanoma (Fig. 3b). Interestingly, the MAPKi-resistant SKMEL28 model maintained JunB protein levels equal to those of their drug-naive melanocytic parents (Fig. 3c). To test whether melanocytic melanoma is specifically vulnerable to switching from a JunB^{low} to a JunB^{high} transcriptional state, we ectopically expressed JunB in the melanocytic SKMEL28 cell lines and found that it robustly induced p21 accumulation when compared with dedifferentiated WM793 cells overexpressing JunB (Fig. 3d). Accordingly, we found that switching melanocytic melanoma from a JunB^{low} to a JunB^{high} transcriptional state inhibited cellular proliferation (Fig. 3e). This finding suggests that molecular characteristics of the drug-naive differentiation state, including vulnerability to JunB induction, are retained following MAPKi resistance and contribute to drug dependence.

To determine whether something about the adaptive dedifferentiation process drives the dependence of SKMEL28 on MAPKi, we ectopically expressed MITF and SOX10 in SKMEL28 models with acquired resistance to BRAF inhibitor monotherapy, MEK inhibitor monotherapy or their combination. MITF activity was functionally

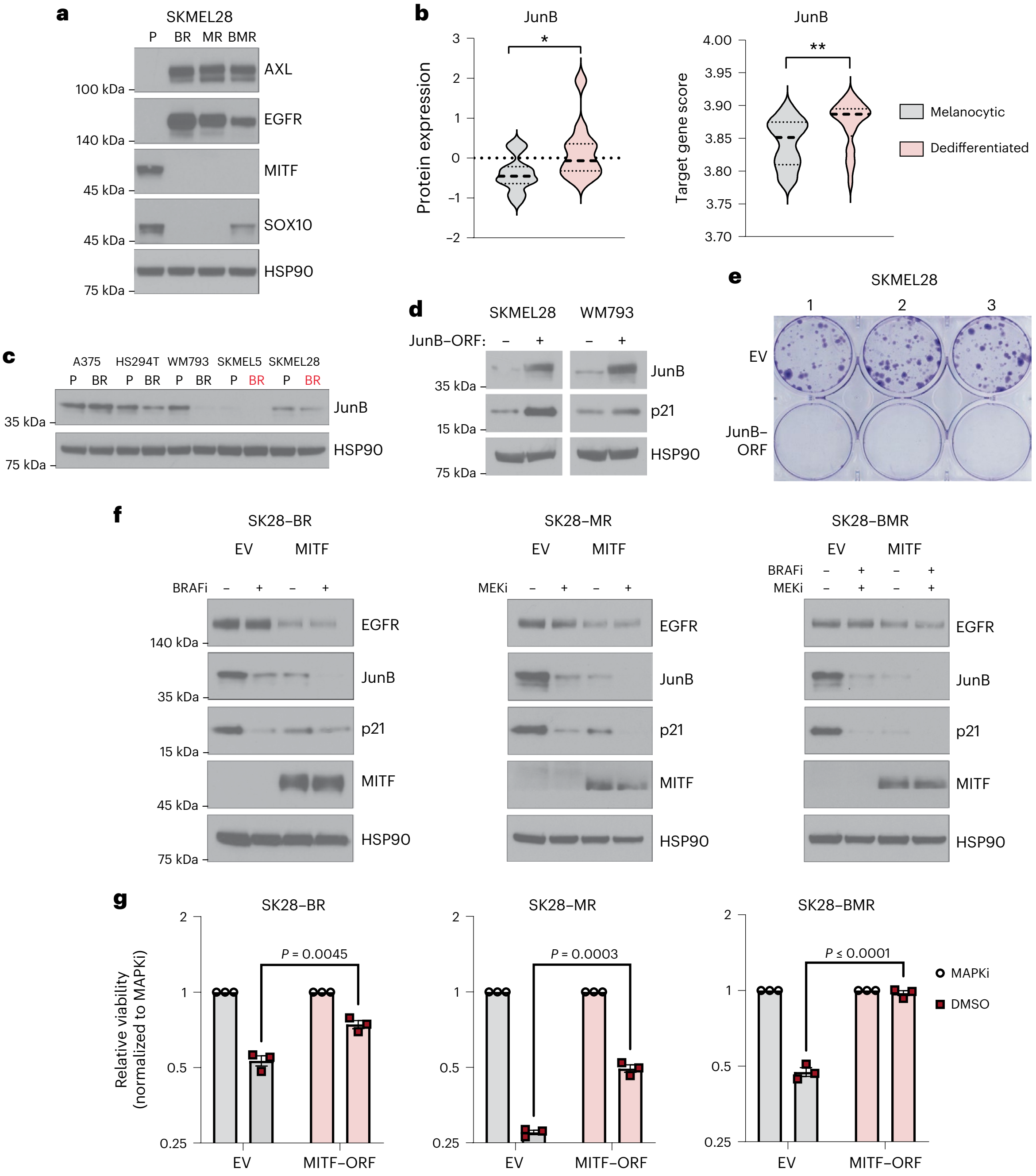

Fig. 3 | Adaptive loss of MITF is a driver of drug dependence in MAPKi-resistant melanoma. a, Western blot analysis of the indicated proteins in parental (P), BR, MR or BMR derivatives of SKMEL28 cells. **b**, Left, JunB-protein-level analysis of melanocytic ($n = 17$) and dedifferentiated ($n = 9$) MAPK-mutant melanoma cell lines using the DepMap Proteomics dataset. Right, JunB target gene expression score across melanocytic ($n = 36$) and dedifferentiated ($n = 26$) MAPK-mutant melanoma cell lines using the DepMap Expression (Public 22Q4) dataset. Two-tailed unpaired t-test, $^{*}P<0.05$ and $^{**}P<0.01$. **c**, Western blot analysis of the indicated protein across the specified P and BR cell lines. **d**, Western blot of SKMEL28 and WM793 parental cells transduced with an EV or JunB expression construction (multiplicity of infection (MOI) = 1). **e**, Clonogenic assay of SKMEL28 cells from experiment **d**. **f**, SK28–BR, SK28–MR and SK28–BMR cell lines were transduced with an EV or a full-length MITF expression vector and treated with DMSO or the indicated MAPKi for 96 h before western blot analysis. **g**, SK28–BR, SK28–MR and SK28–BMR were transduced with an EV or a full-length MITF (MITF–ORF) expression vector. After selection, the cell lines were seeded at 10,000 cells per ml and treated with DMSO or the specific MAPKi therapy to which they evolved resistance. The drug was refreshed every 72 h. After 10 days, the cells were counted, and the MAPKi counts were normalized to the DMSO counts. Two-tailed unpaired t-test; P values included in the figure. Data are presented as mean ± s.e.m. In **a** and **c**–**g**, these data represent three independent experiments ($n = 3$).

confirmed by observing its inhibition of EGFR expression (Fig. 3f)[40]. Following the withdrawal of MAPKi, MITF expression, but not SOX10 expression, entirely blocked the induction of the JunB–p21 signalling axis (Fig. 3f and Supplementary Fig. 2f). MITF expression also rescued the inhibited cell growth following the withdrawal of MAPKi in resistant SKMEL28 models (Fig. 3g). Together, these mechanistic data show that the loss of MITF in melanocytic differentiated melanomas facilitates not only dedifferentiation and drug resistance but also JunB–p21-dependent growth inhibition following drug-removal-induced ERK hyperactivation.

Drug holidays can minimize growth in drug-dependent models

The poor growth of drug-dependent resistant cells in drug-free environments suggests that population growth may be minimized by incorporating drug-free 'holidays' into treatment schedules[7,45]. However, heuristics guiding the proper design of optimal drug holiday regimens need to be clarified, as these may depend on the population's initial properties (for example, the ratio of sensitive to resistant cells) and the growth characteristics of different subpopulations. To investigate this question, we seeded a growth experiment with a panel of BRAFi-resistant (BR), MEK inhibitor (MEKi)-resistant (MR) or BRAFi- and MEKi-resistant (BMR) *BRAF*$^{\mathrm{V600E}}$ melanoma cell lines. The resistant cells were mixed at a 9:1 ratio with their matched parental cells, loosely mimicking a progressing tumour that has become dominated by resistant cells. We then measured population size in each population after 9 days of exposure to 1 of 3 different treatment schedules: (1) 100% DMSO ('drug off'), (2) 100% MAPKi ('drug on') or (3) a random intermittent therapy in which MAPKi was applied 30% of the time. We found that the periodic dosing schedules outperformed either the drug-free or the drug-only treatments, but not both. Specifically, total population size was minimized by schedule 3 in the populations containing drug-dependent (SK28–MR and SK28–BMR) resistant subpopulations and by schedule 2 in the populations with non-dependent resistant subpopulations (A375–MR and WM793–BR; Fig. 4a). To investigate whether a more judiciously chosen treatment schedule may further reduce growth, we considered a simple mathematical model of exponentially growing subpopulations (sensitive and resistant cells) whose growth rates depend on the environment (with or without drugs; Supplementary Information). On long timescales, we expect static treatments to eventually select the subpopulation with the highest growth rate in that environment. However, in the presence of time-dependent treatments that switch between drug and no-drug epochs, it may be possible to maintain a heterogeneous population of both cell types—each one suboptimal in one environment and optimal in the other—that leads to reduced growth of the total population. Indeed, in the limiting case in which cells do not interact, a treatment strategy will maintain coexisting populations of both cell types when the drug treatments comprise a fraction (f_{on}) of the total treatment time T

$$f_{\mathrm{on}} = \frac{1}{1+\gamma} \tag{1}$$

where $\gamma \equiv \frac{k_{1,\mathrm{on}} - k_{2,\mathrm{on}}}{k_{2,\mathrm{off}} - k_{1,\mathrm{off}}}$ is a dimensionless parameter that depends only on the growth characteristics ($k_{i,\mathrm{on}}$ and $k_{i,\mathrm{off}}$) of the different subpopulations; $k_{i,\mathrm{on}}$ ($k_{i,\mathrm{off}}$) is the per capita growth rate of population i in the presence (absence) of the drug. The value of $k_{i,\mathrm{on}}$ depends on the concentration of the drug, which we assume is fixed throughout the experiment (during all 'on' epochs). More generally, the parameter values ($k_{i,\mathrm{on}}$ and $k_{i,\mathrm{off}}$) will depend on drug concentration, cell line and culture conditions, but they are straightforward to measure in a given experiment. In our experiments, we choose a particular drug concentration up front and directly measure the growth parameters ($k_{i,\mathrm{on}}$ and $k_{i,\mathrm{off}}$) for those conditions. We then assume that these parameters remain fixed throughout the experiment (that is, $k_{i,\mathrm{on}}$ and $k_{i,\mathrm{off}}$ are independent of time, but we relax these assumptions below). This simple model suggests that we can maintain population heterogeneity by incorporating drug-free epochs when $\gamma > 0$, that is, when sensitive cells grow faster than resistant cells without the drug, while resistant cells grow faster than sensitive cells with the drug. In the long-term limit ($T \to \infty$), this treatment strategy yields a constant ratio of the different cell types, independent of the initial composition of the population. In addition, the growth of this heterogenous population is optimal; that is, it is smaller than growth in either static with-drug or static drug-free environments if

$$\begin{aligned} k_{2,\mathrm{on}} - k_{2,\mathrm{off}} &> 0 \\ k_{1,\mathrm{off}} - k_{1,\mathrm{on}} &> 0 \end{aligned} \tag{2}$$

Equation (2) shows that one cell type ($i = 2$) must grow faster with the drug than without, while the other cell type ($i = 1$) must grow faster without a drug than with; these are the precise conditions that define drug-dependent resistance. In summary, in this simple model, one can maintain heterogeneity as long as sensitive cells are favoured during drug-free epochs. Furthermore, that heterogeneity leads to minimal growth only when the resistant cells grow faster with the drug than without (that is, when they are drug dependent). Importantly, the model predicts an optimal treatment that is highly dependent on (experimentally accessible) growth rates, which depend on the cell line, drug concentration and environment.

Equation (1), along with experimentally measured growth rates of parental and resistant lines with and without the drug, predicts an optimal schedule with $f_{\mathrm{on}} = 0.29$ (holiday 71% of the time) for the SKMEL28 (drug dependent) population and $f_{\mathrm{on}} = 1$ (drug only) for the A375 (non-dependent) population. Based on these predictions, we experimentally compared five different treatment schedules: (A) 100% drug off ($f_{\mathrm{on}} = 0$), (B) 100% drug on ($f_{\mathrm{on}} = 1$), (C) a random schedule, (D) an optimal schedule with $f_{\mathrm{on}} \approx 0.29$ where the drug was given for 2.6 days on followed by 6.4 days off and (E) an optimal schedule with $f_{\mathrm{on}} \approx 0.29$ where the drug was given for 1.1 days on, 5.5 days off, 1.5 days on and 0.9 days off. Consistent with predictions of the model, the optimal schedules (D and E) outperformed other treatments in the populations with drug-dependent resistance (SK28–BR) but were outperformed (by schedule B) in the populations with non-dependent resistance (A375–BR; Fig. 4c). We found no significant difference between schedules D and E, consistent with the fact that schedules should depend only on f_{on} (not the specific timing of the holidays) when subpopulations are acting approximately independently.

Fig. 4 | Scheduling drug exposure can optimize growth inhibition in dependent cell lines. a, A375–MR, WM793–BR, SK28–MR and SK28–BMR cell lines were mixed with their parental counterparts at a ratio of 18,000 resistant to 2,000 parental cells and were treated with 1 μM of drug as described for 9 days before counting. Two-tailed unpaired *t*-test; *P* values are included in the figure. Drug-dependent cell lines are shown in red. **b**, Schematic of five different drug schedules: (A) 100% drug off (DMSO), (B) 100% drug on (1 μM PLX4720), (C) random periodic schedule, (D) optimal schedule up front and (E) optimal schedule split into two epochs. **c**, Left, 2,000 parental and 18,000 SK28–BR cells. Right, 2,000 parental and 18,000 A375 BRAFi-resistant cells treated according to the schematic in **b**. On the ninth day, cells were counted. One-way ANOVA with Tukey's multiple-comparison test. NS, not significant; $^{*}P < 0.05$; $^{***}P < 0.01$; $^{****}P < 0.0001$. The data represent nine independent experiments ($n = 9$). **d**, SKMEL28 parental (EGFR$^{\mathrm{null}}$) and BRAFi-resistant (EGFR$^{\mathrm{high}}$) populations were mixed and treated with continuous DMSO (100% drug off) or continuous 1 μM PLX4720 (100% drug on) for 20 days before splitting into the specified drug treatment schedule. Left, cell surface expression of EGFR$^{\mathrm{high}}$ populations on every split day of the experiment. Right, estimated cell counts on every split day of the experiment. **e**, Empirically constrained simulations show the optimal fraction of time exposed to the drug as the ratio of sensitive to drug-dependent cells and total treatment time is varied. **f**, Algorithm-predicted optimal percent drug holiday as total treatment time increases. The optimal asymptote is represented by a dashed line. **g**, A mixture of 2,500 parental and 7,500 SKMEL28 BRAFi-resistant cells was treated with the indicated schedule of 1 μM PLX4720 24 h later. The algorithm-predicted optimal ('winning') schedule is indicated along the *x*-axis, and time points that conform to predicted values are indicated with an asterisk. In **a**, **d** and **g**, these data represent three independent experiments ($n = 3$). In **a**, **c**, **d** and **g**, data are presented as mean ± s.e.m.

To further understand the effectiveness of optimal therapy scheduling at forestalling resistance, we created a mixed population of resistant–dependent (~43%) and parental (~57%) SKMEL28 cells. Long-term population dynamics were tracked by cell surface expression of EGFR, with EGFR^{high} status indicating the dependent–resistant population (Fig. 4d, left). Following 20 days of continuous PLX4720 treatment, the population was ~95% resistant–dependent cells (Fig. 4d, left), and at this point, we split this population into treatment groups that used 40% drug (optimal schedule, $f_{on} = 0.4$) or 100% drug ($f_{on} = 1$). The optimal-schedule group remarkably slowed population growth (Fig. 4d, right).

The optimal schedule is dependent on the treatment length

On sufficiently long time horizons, we expect that the optimal treatment will be independent of the initial composition of the tumour. However, many real-world applications will probably involve finite-time

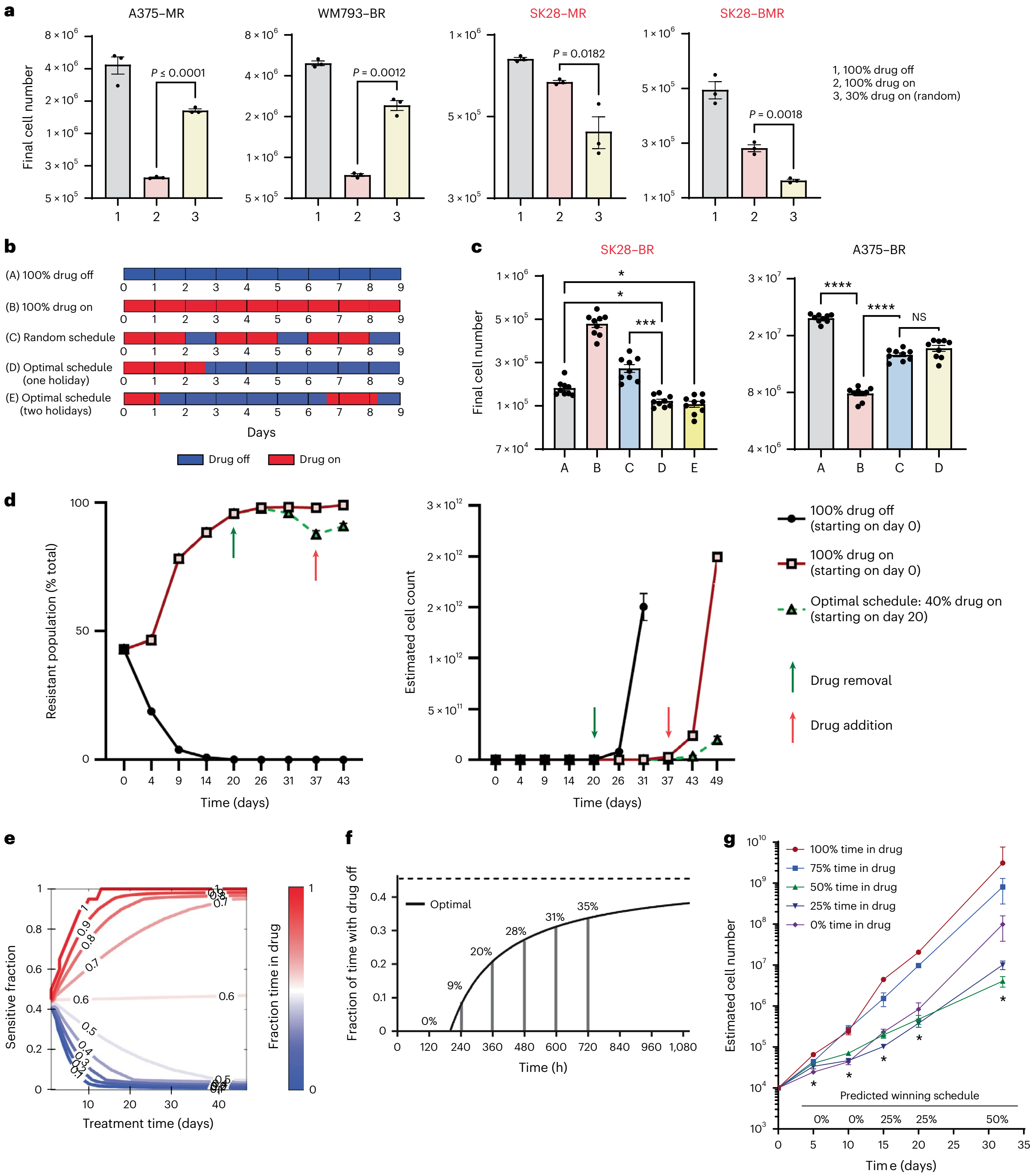

treatments in which these asymptotic results are invalid. Under these conditions (Supplementary Information), the growth of the population will be minimized when

$$f_{\mathrm{on}} = \frac{1}{1+\gamma} + \frac{1}{T}\log\left(\frac{n_1(k_{1,\mathrm{off}} - k_{1,\mathrm{on}})}{n_2(k_{2,\mathrm{on}} - k_{2,\mathrm{off}})}\right) \quad (3)$$

Equation (3) reduces to equation (1) when $T\to\infty$. However, on shorter time horizons, the optimal treatment will depend on the total treatment duration T (Fig. 4e). To test this prediction experimentally, we plated a mixed population of 10^5 cells comprising 25% resistant–dependent SKMEL28 cells. The cells were treated with one of five schedules with drug holidays ranging from 0 (static with-drug treatment) to 100% (static drug-free treatment). The treatment schedules were broken into 5 day blocks so that the cells could be counted every 5 days for an indeterminate length of time and remain on schedule. Based on the results of the model (Fig. 4f), we hypothesized that the treatment performing optimally would vary over time, with static drug treatments minimizing growth at early times and treatments with increasing drug holidays (asymptotically approaching the long-time optimum of approximately 45% drug holiday, $f_{\mathrm{on}} = 0.55$) minimizing growth on longer timescales.

Indeed, experiments confirmed that growth was initially (for example, days 5 and 10) minimized in the static drug (PLX4720) treatment (Fig. 4g). However, by day 15, the treatment with 25% holiday ($f_{\mathrm{on}} = 0.75$) was optimal, while the treatment with 50% drug holiday—which most closely corresponds to the predicted long-time optimum—led to minimal growth by day 30. These results underscore the notion that the optimal strategy for drug holidays will initially vary over time—a phenomenon tied to the transient behaviour of the population as it approaches a steady-state composition—but for sufficiently long treatment periods approaches an optimum that is independent of the initial population composition.

Presence of non-dependent resistant cells does not alter optimality

Because parental melanoma tumours potentially give rise to both drug-dependent and non-dependent resistant lineages, we asked how the presence of both resistance types would impact the optimal treatment schedule. To answer this question, we subjected two different mixed populations containing drug-sensitive, drug-resistant dependent and drug-resistant non-dependent derivatives of UACC62 to one of three treatments: (1) static drug-free treatment, (2) static treatment with PLX4720 or (3) a model-inspired (approximately) optimal treatment with $f_{\mathrm{on}} = 0.45$ (55% of the time in drug holiday). The two mixed populations comprised approximately constant ratios of drug-sensitive to drug-dependent resistant cells. However, one population initially contained 0.2% non-dependent resistant cells and the other 10% non-dependent resistant cells. In both populations, the model-inspired therapy—which contains drug holidays calculated without knowledge of the non-dependent populations—significantly outperformed the static therapies (Fig. 5a), as one might intuitively expect. However, the population sizes become much larger in populations that started with more non-dependent resistant cells, consistent with predictions of the model (Fig. 5b). This result highlights a more general principle: in cases in which non-dependent resistant cells grow at similar rates in the presence and absence of the drug, these cells are not expected to alter the choice of optimal therapy. However, their presence can limit the utility of intermittent therapy in cases in which these cells grow faster than the average growth rate of the drug-holiday-optimized population of sensitive and drug-dependent cells.

Adaptive therapy based on population size approximates optimal schedule

In a clinical setting, detailed measurements of growth parameters for different cell types are not typically possible. Therefore, we attempted to develop an adaptive therapy method that approximates the optimal holiday schedule without detailed growth rate information about the individual subpopulations (Fig. 5c and Methods). Briefly, we began by administering the drug for one treatment window, followed by the removal of the drug for one treatment window. The growth rates of each treatment window were recorded, and the treatment that led to a lower growth rate was then continued. This treatment protocol was continued until the growth rate of the population surpassed that of the opposite treatment type, as recorded by the most recent treatment window of that type. At that time, the treatment is switched. This process continued until the treatment ended.

We tested the performance of this approach computationally using empirically measured growth rates from the previous experiments (Fig. 5d). Simulations revealed that the performance of the blind adaptive therapy approaches that of true optimal therapy, provided that one can make sufficiently frequent measurements of total population size. To test this approach experimentally, we established a mixed population comprising sensitive and resistant dependent SKMEL28 cells and exposed replicate populations to one of four drug schedules: (1) static no-drug schedule ($f_{\mathrm{on}} = 0$), (2) static PLX4720 (constant drug) schedule ($f_{\mathrm{on}} = 1$), (3) the optimal schedule ($f_{\mathrm{on}} = 0.6$, 40% drug holiday) based on measured growth rates of the different cell populations and (4) the adaptive schedule described above. Treatments were applied in 4 day blocks for a total of 48 days. As predicted by the model, the optimal therapy (treatment 3) performed considerably better than the two static therapies. In addition, the adaptive therapy and the calculated optimal schedule performed almost identically over 48 days (Fig. 5e,f). To determine if we had achieved the goal of maintaining population heterogeneity, we took the final cell population from each schedule and measured the concentration which inhibited 50% of population growth (GI_{50}) of each population to PLX4720 (Fig. 5g). As a benchmark, we compared these GI_{50} values to those of freshly made mixtures containing 100% sensitive, 50% sensitive and 50% resistant, and 100% resistant populations. We found that the populations treated with 0% PLX4720 (100% PLX4720) exhibited GI_{50} values similar to those of fully sensitive (resistant) populations, consistent with the prediction that static therapies eventually lead to homogeneous populations (Fig. 5g, blue and red bars). By contrast, populations treated with the optimal schedule exhibited GI_{50} values similar to, but slightly smaller than, those of an equally mixed population of 50% sensitive and 50% resistant cells (Fig. 5g, grey bars). These results suggest that reaching near-optimal treatment outcomes with incomplete population dynamics information may be possible.

Well-mixed model approximates an agent-based model

The 'well-mixed' model above neglects complicating features—for example, stochasticity, cell death and turnover, and spatial competition—that may be necessary to predict scheduling in a more realistic in vivo environment. To explore how these features impact our predictions, we implemented a 2D, on-lattice, agent-based model (ABM; Methods). We began with a sparsely seeded, mixed population of sensitive and drug-dependent resistant cells. Each population divides with an effective proliferation rate informed by their birth rate (determined by in vitro experiments) and a constant death rate to simulate in vivo cell turnover. We then simulated a variety of drug holiday schedules (Fig. 6a,b). Simulations that used a drug holiday similar to the predicted optimum led to a smaller tumour population at the end of a 9 day simulated treatment (Fig. 6b), consistent with predictions of the simpler model. The success of the simple model is not altogether unexpected because it predicts that the optimal f_{on} depends only on a ratio of growth rate 'differences', not the absolute values. As a result, environmental factors that impact all cell types approximately equally—for example, by scaling all growth rates by a constant factor—will not change the predicted optimum.

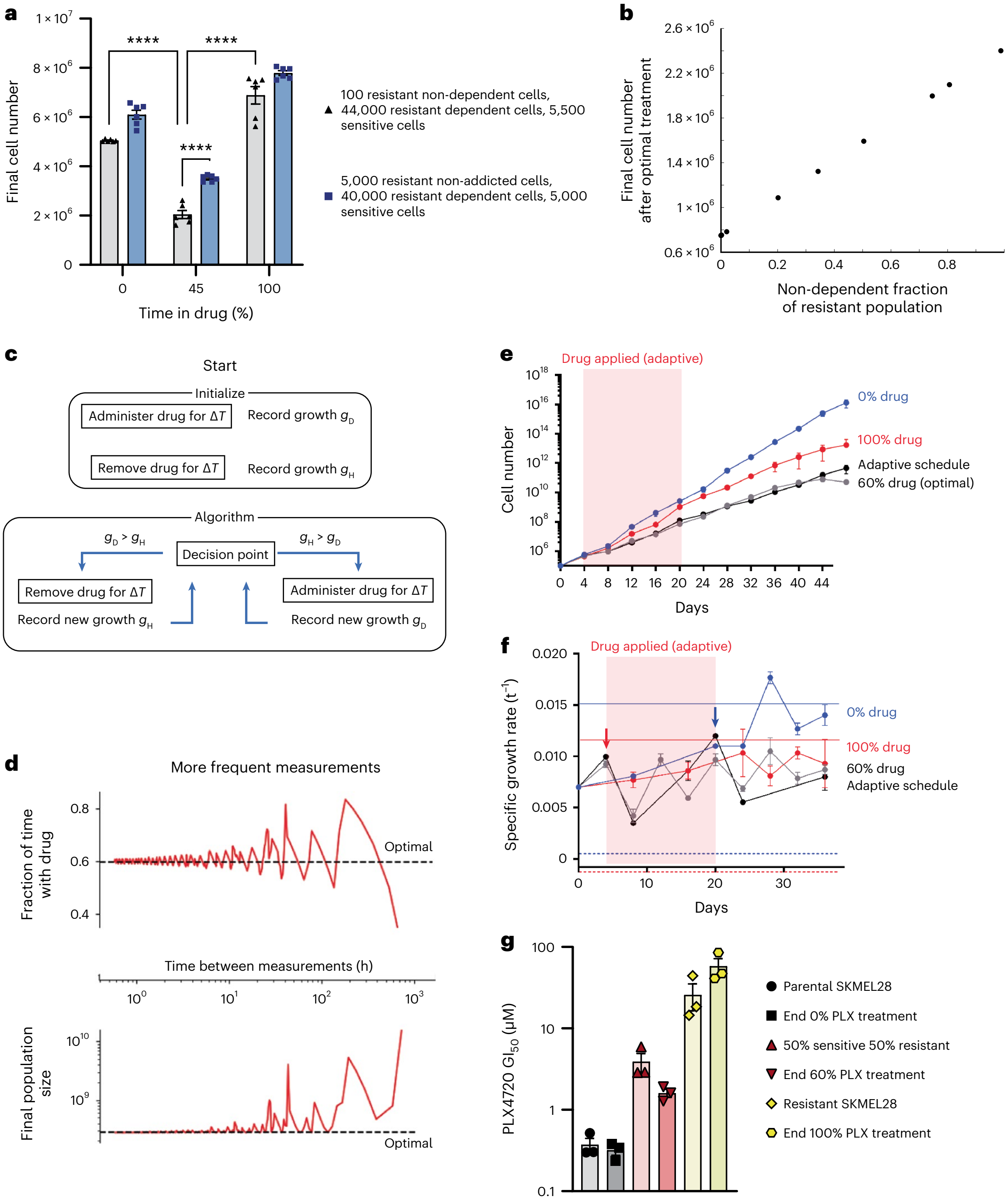

Fig. 5 | Optimal scheduling can be approximated with a mixed cell population of unknown growth rates. a, A mixture of the specified ratios of UACC62 cells was treated with 1 μM PLX4720 at the indicated schedules 24 h later. Cells were counted on day 9. One-way ANOVA with Tukey's multiple-comparison test. ****$P < 0.0001$. The data represent six independent experiments ($n = 6$). **b**, Using empirically constrained simulations, we plot the total population count as the fraction of non-dependent resistant cells varying from 0% to 100% of the resistant population. **c**, A cartoon schematic of the blind adaptive therapy algorithm where g_D is the growth in drug and g_H is the growth during a holiday. **d**, Top, using empirically measured growth rates, we simulate the fraction of time spent exposed to a drug following the blind adaptive therapy (red solid line) and compare it with the true optimum (black dashed line) as a function of how frequently population-level growth rates can be measured. Bottom, the same simulations as above but the final cell count of the population (red solid line) is compared with what is projected from the optimal schedule (black dashed line). **e**, Results of the blind adaptive therapy experiment. Cell counts over time were recorded, and the shaded red region highlights the time the drug was applied. **f**, Growth rates for each schedule at the indicated time points. The growth rate of parental SKMEL28 cells in DMSO (blue solid line) and BRAFi (blue dashed line) is indicated. Arrows indicate time points when the treatment condition was changed because of the measurement. The growth rate of PLX-resistant pooled SKMEL28 cells in 1 μM PLX4720 (red solid line) and DMSO (red dashed line) is indicated. The red region highlights the period the drug was applied. **g**, The PLX4720 GI_{50} values of the ending cell populations in **e** compared with the PLX4720 GI_{50} values of the indicated known mixtures of parental and resistant SKMEL28 cells. The data in **e** and **g** represent three independent experiments ($n = 3$). The data in **a** and **e**–**g** are presented as mean ± s.e.m.

https://doi.org/10.1038/s41559-023-02255-x

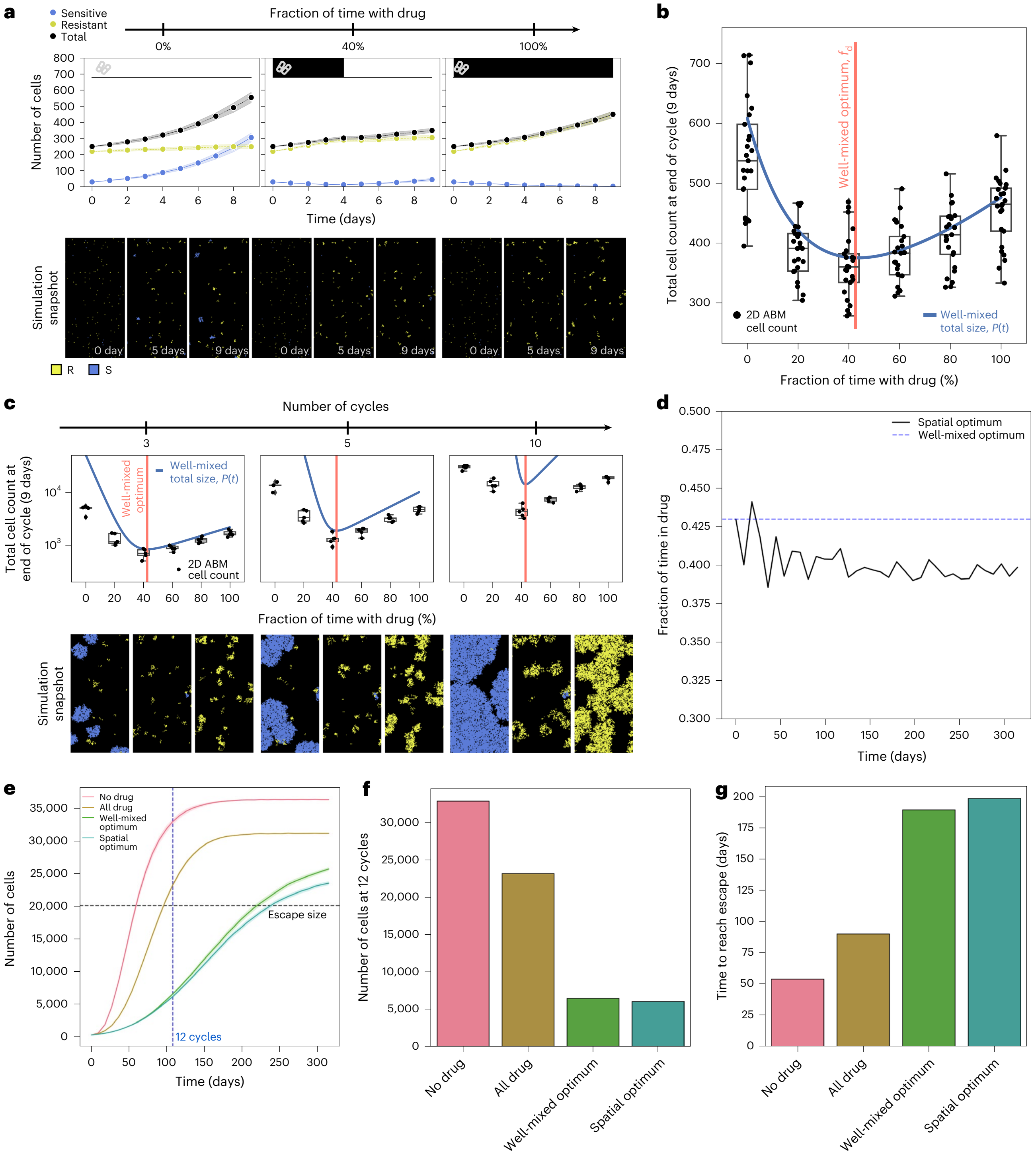

Fig. 6 | Optimal schedules derived from a well-mixed model approximate those derived from an ABM incorporating cell turnover, spatial competition and carrying capacity. a, Representative ABM simulations depicting 0% drug treatment, 40% drug treatment and 100% drug treatment schedules for one drug cycle, or 9 days. Blue cells and lines represent sensitive cells, and yellow cells and lines represent resistant and dependent cells. Cell death and turnover are equal for all cell types and drug concentrations and are equal to half the sensitive populations' drug-free growth rate. **b**, Similar to **a** but with 25 replicates and additional treatment schedules (0%, 20%, 40%, 60%, 80% and 100% time in drug). ABM simulations (black dots, box and whisker plots) show broad agreement with the well-mixed experimental model prediction (blue line). The predicted well-mixed optimum (red vertical line) captures the simulations well. **c**, Simulations similar to **a** and **b**, but the simulations continue for three, five and ten cycles of treatment (each cycle is one 9 day schedule). **d**, Using the data from **c**, we calculate the optimal treatment after each 9 day treatment schedule and how it varies as the populations compete for space. This result is deemed the 'spatial optimum'. **e**, Simulations comparing the total population size over time using the well-mixed optimum, spatial optimum, 100% drug and 0% drug. **f**, Comparison of total cells after 12 cycles (blue dashed line in **e**; the last cycle before the worst condition reaches carrying capacity) reveals an ~8% decrease in cell count of the spatial optimum compared with the well-mixed optimum. **g**, Comparison of the time to reach treatment escape (grey horizontal dashed line in **e**) reveals that the spatial optimum extends treatment success for an additional ~8%. In **b** and **c**, box plot elements are defined as follows: centre line, median; box limits, upper and lower quartiles; whiskers, 1.5× interquartile range.

We next investigated simulations over longer treatment periods, in which cell crowding may introduce non-intuitive effects. We repeated the previous experiment but administered treatment for three, five and ten 9 day cycles. We found that the optimal treatment schedule remains optimal across all treatment lengths, but the final tumour burdens predicted by the well-mixed model become increasingly inaccurate (Fig. 6c). Deviations between the ABM and the well-mixed model appear well before the tumour reaches carrying capacity (Supplementary Fig. 3a), suggesting that the effect is due to local cell crowding, similar to what occurs in other tumour models[46].

During each 9 day optimal cycle, the population experiences one epoch in drug and one without. As a result, each 9 day cycle allows us to extract effective growth rates ($k_{i,\mathrm{on}}$ and $k_{i,\mathrm{off}}$) for the previous period; with these measurements, we can therefore calculate the (now time-dependent) optimal drug dose $f_{\mathrm{on}}(t)$ for each 9 day period (Fig. 6d, black line). As expected, the time-dependent optimum initially agrees with the well-mixed optimum (Fig. 6d, blue dashed line), but over time, the optimum requires less drug than predicted by the simple model (Supplementary Fig. 3b). We confirmed that the optimum, $f_{\mathrm{on}}(t)$, calculated in this way, indeed outperforms the static, well-mixed optimum (Fig. 6e–g). To compare performance between optimal treatments prescribed by the well-mixed and spatial models, we compared total population sizes across treatment arms after 12 cycles (108 days, the last cycle before carrying capacity is reached in the largest population; Fig. 6e, blue vertical dashed line). In addition, we measured how long each treatment arm contained the population below a given threshold ('escape size') for the first time (Fig. 6e, grey horizontal line). Across both tests, we found that the spatial optimum outperformed the well-mixed optimum by approximately 8% (Fig. 6f,g).

Discussion

Our work complements a broad set of recent studies ranging from purely theoretical evolutionary therapy to clinical trials that have attempted to harness intermittent drug treatment schedules. Importantly, it shows that while drug holidays can improve tumour growth control, they must be designed and implemented using strategies such as the adaptive treatment regimen described here, which account for the evolutionary dynamics of cells within the tumour—which harbour potentially different drug response and dependency characteristics—as well as the variation in these properties across individual patients. In addition, this work suggests that the heterogeneity of differentiation states found in melanoma tumours is a predictive and mechanistic factor associated with drug dependence in MAPK-mutant melanoma. The lack of incorporation of these elements may be at least partially responsible for the failure of recent trials regarding intermittent therapy[10,47]. Together, these findings support melanocytic tumours as prime candidates for optimized, intermittent MAPKi therapy to slow disease progression when other options are unavailable.

Interestingly, MITF loss has previously been described in the literature as a contributing factor to MAPKi addiction in melanoma models[9]. In that report, it was discovered that withdrawal of MAPKi from drug-dependent models activated ERK2–JunB, which led to subsequent loss of MITF protein and cell cycle arrest. In this scenario, drug resistance emerging in melanocytic differentiated models that have remained in this differentiation state during the acquisition of resistance is associated with drug-removal-induced MITF loss. Indeed, we observed this proposed mechanism in BRAFi-resistant SKMEL5 cells upon withdrawal of MAPKi (Supplementary Fig. 2g). In our study, we describe a distinct scenario in which melanocytic differentiated melanoma cells undergo MITF loss and associated dedifferentiation during the acquisition of drug resistance, and we show that such cells retain sensitivity to ERK-hyperactivation-induced JunB–p21 activation (Supplementary Fig. 4). Both cases underscore the notion that MITF is a key regulator of the drug-dependence phenotype, supporting our discovery that melanocytic melanoma tumours are primed for MAPKi addiction.

To capture more potential features of in vitro evolution such as stochasticity, cell death and turnover, spatial competition and carrying capacity, we translated our system into a 2D, on-lattice ABM. We found, somewhat unexpectedly, that predictions from the simple model were largely robust against these additional complexities. Specifically, we observed that cell death and turnover did not affect the optimal schedule, as long as the intrinsic turnover rate was approximately equal for each cell type. In addition, the well-mixed model perfectly recapitulated the results from the spatial simulations at low densities, but at large densities, we observed an asymmetric impact on growth rates that led to modest changes in the optimal treatment schedule—a schedule we could infer by updating the estimates of cell growth rates over time. This time-dependent ABM optimal schedule led to an approximately 8% decrease in tumour size as well as 8% increase in population escape time over the well-mixed optimum. Taken together, these results suggest that while spatial effects can play an important role in fine-tuning the optimal schedule, the well-mixed model remains an unexpectedly accurate approximation for our experimental system.

It is also important to address several potential limitations in our approach. For example, our models ignored the potential impacts on drug resistance from the host environment, specific resistance mutations and ecological interactions within the tumour. In addition, we ignore the role of de novo mutations in evolutionary adaptation, which would probably play a role in informing the optimal treatment, at least in small populations (see Supplementary Information for a brief discussion on mutation rates). However, even in this well-controlled laboratory setting, calculating an optimal schedule is challenging. As a result, it is notable that such a simple mathematical model captures the main qualitative features necessary to define optimal therapy schedules. Furthermore, it is significant that empirical adaptive scheduling can produce near-optimal results when frequent tumour growth surveillance is performed, a concept that is becoming increasingly feasible with the broad adoption of minimally invasive, blood-based monitoring of circulating tumour DNA levels. To be clear, the model in its current form is not meant to be directly applicable in the clinic. But its unexpected success in in vitro and in silico experiments—which already include numerous biological complexities neglected in the model—gives hope that similarly simple 'minimal' models may aid in understanding which melanoma tumours are primed for drug dependence and how one might optimally treat such tumours in realistic clinical scenarios. Finally, although holiday-based schedules cannot entirely prevent disease progression, they are a promising therapeutic approach to slow progression, which may eventually lead to improved treatment outcomes for a subset of patients with drug-dependent metastatic disease.

Methods

Cell lines

A375, COLO679, UACC62, WM793, HS294T, SKMEL5 and SKMEL28 cells were grown in RPMI 1640 (Life Technologies) supplemented with 10% FBS (Sigma–Aldrich) and 1% penicillin and streptomycin (Life Technologies). SKMEL28 cell lines were obtained from L. Garraway (Dana–Farber Cancer Institute, Harvard University). All other cell lines were purchased from the American Type Culture Collection. All lines were submitted to short tandem repeats (STR) profiling by the Duke University DNA Analysis Facility to confirm their authenticity. The cells routinely tested negative for mycoplasm with the MycoAlert Mycoplasma Detection Kit (Lonza number LT07-318).

Chemicals

All inhibitors were purchased from Selleck Chemicals and prepared at 100 mM stock solutions in DMSO.

GI_{50} assay

Wherever GI_{50} values of specific inhibitors are indicated, they were determined as follows. Cells were seeded at 5,000 cells per well in

96-well plates in normal tissue culture conditions. After a 24 h incubation, diluent (typically DMSO) or concentrated 10-fold dilutions of the indicated inhibitors (at 1:1,000) were added to the cells to yield the highest concentration of 200 µM (all other inhibitors). After a 3 day incubation with the treatment, cell viability was assessed with the CellTiter-Glo luminescent viability assay (Promega) according to the manufacturer's instructions. Growth inhibition was calculated as a percentage of diluent-treated cells, and GI_{50} values were determined to correspond to the inhibitor concentration that resulted in half-maximal growth inhibition.

Immunoblotting

The western blot procedure was followed as previously described[48]. Primary antibodies were all purchased from Cell Signaling Technology and diluted at 1:1,000. The catalogue numbers are as follows: phospho-ERK (9101), ERK (4695), EGFR (4267), PARP (9542), vinculin (4650), beta-actin (4970), AXL (8661), p75NTR (4201), MITF (12590), SOX10 (89356), SOX9 (82630), JunB (3753), p21 (2947), HSP90 (4874), FRA1 (5281) and p-FRA1 (3880).

Cell surface flow cytometry

Pelleted cells were resuspended in 100 µl of flow cytometry staining buffer (eBioscience, number 00-4222-26) at a concentration of 100,000 cells per ml. Allophycocyanin (APC) anti-human EGFR antibody (Biolegend, number 352906) or APC Mouse IgG1, κ Isotype Ctrl (FC) Antibody (Biolegend, number 400122) was added at 2,000× to the suspended cells, and the reaction was left to incubate at room temperature for 30 min. Cells were washed thrice with 1 ml of flow cytometry staining buffer. Data were acquired with a FACSCanto II (BD Biosciences) flow cytometer, and the results were analysed in Flowjo (TreeStar).

Lentivirus preparation and DNA constructs

All expression plasmids were prepared in lentiviral form as previously described[49]. In brief, expression constructs, psPAX2 (Addgene, number 12260) and pMD2.g (Addgene, number 12259) were transfected into AAVpro 293Ts (Takara, number 632273) using Lipofectamine 2000 (Thermo Fisher Scientific, number 11668500) according to the manufacturer's protocol. Following a 4 h incubation, the transfection medium was removed and replaced with harvest medium containing 30% FBS. The virus-containing medium was collected after 48 h or 72 h, filtered with a 0.45 µm filter and stored at −80 °C until use with 8 µg ml^{-1} polybrene (Sigma–Aldrich). pHAGE-EGFR was a gift from G. Mills and K. Scott (Addgene plasmid number 116731; http://n2t.net/addgene:116731; Research Resource identifier (RRID): Addgene_116731). pHAGE_puro was a gift from C. Vakoc (Addgene plasmid number 118692; http://n2t.net/addgene:118692; RRID: Addgene_118692). FUW-Sox10 was a gift from B. Weinberg (Addgene plasmid number 36978; http://n2t.net/addgene:36978; RRID: Addgene_36978). TFORF2346 was a gift from F. Zhang (Addgene plasmid number 142043; http://n2t.net/addgene:142043; RRID: Addgene_142043).

Generation of CRISPR/Cas9 knockouts

lentiCRISPR v2 was a gift from F. Zhang (Addgene plasmid number 52961; http://n2t.net/addgene:52961; RRID: Addgene_52961). Single guide RNAs (sgRNA) were chosen from the TKOv3 genome-wide library[50] (JunB-1: GTGTAGAGAGAGGCCACCAG and JunB-2: ACTCCTGAAACCGAGCCTGG) and were cloned into lentiCRISPR v2 using the protocol provided by the maker. Lentivirus containing the plasmid was generated as described above. Cells were spinfected with a mixture of virus, 8 µg ml^{-1} polybrene and medium at 2,250 rpm for 1 h, followed by incubation at 37 °C overnight in the transduction mixture. The following day, the transduction mixture was removed and 2 µg ml^{-1} of puromycin was added to the cells. After 48 h, the surviving cells were seeded into the described experiments.

In vitro adaptation of inhibitor-resistant cells

PLX4720-, AZD6244-, or PLX4720- and AZD6244-resistant cell lines were produced using one of two methods as previously described[49]. Briefly, parental cells were either exposed to escalating inhibitor doses or exposed to a high dose (3 µM) of inhibitor until logarithmic growth resumed. The resultant resistant clones were expanded and cultured. Parental cell lines were cultured concurrently with DMSO. Resistant cell lines were maintained in routine culture with 3 µM MAPKi drug. All resistant and DMSO parental control lines were submitted to short tandem repeat (STR) profiling by the Duke University DNA Analysis Facility to confirm their authenticity upon the acquisition of resistance.

Clonogenic growth assay

To measure the ability of cell lines to form colonies from a single cell, clonogenic growth assays were performed as previously described[49]. Briefly, 1,000–5,000 cells were seeded per well in 6- or 12-well tissue culture plates in standard growth medium. After 24 h, the indicated treatments were added, and the assay was incubated for 14–21 days with fresh medium and inhibitors every 72–96 h. Cells were fixed and stained with 0.5% (w/v) crystal violet in 6.0% (v/v) glutaraldehyde (Thermo Fisher Scientific). Quantifications of the surface area covered were used to estimate cell viability and were performed in ImageJ software with the ColonyArea plugin[51].

Cell cycle analysis

To analyse the progression of cells through the cell cycle, cells were plated in triplicate at 20,000 cells per well in six-well plates. The following day, the growth medium was removed and replaced with fresh medium containing the indicated dose of drug or diluent (typically DMSO). After a 72 h incubation in the drug, cells were counted. The cells were washed twice in PBS and stained with a solution of 50 µg $µl^{-1}$ RNase A, 20 µg $µl^{-1}$ propidium iodine and 0.05% TritonX-100 in PBS (Sigma–Aldrich). Around 1×10^6 cells were washed twice with PBS and then fixed in 70% ethanol. The DNA content of the cell population was determined and quantified using flow cytometry. Gating was defined using untreated and unstained cells, and treatments were evaluated at 20,000 counts using BD FACSVantage SE.

Senescence-associated β-gal assay

To determine the effect of treatment on the induction of senescence, cells were plated in triplicate in 6-well plates at a density that would achieve 80–90% confluency at 10 days of growth, typically between 1,000 and 50,000 cells. After 24 h of culture, the growth medium was removed and replaced with fresh medium containing the indicated drug or diluent. After 10 days of treatment, the medium was removed and the cells were stained with the Senescence β-Galactosidase Staining Kit (Cell Signaling Technology), according to the manufacturer's instructions. Bright-field images were taken at 100× magnification at 5 random locations in each well. Representative images are shown.

DepMap analyses

Addictive versus non-addictive RNA-sequencing comparison. Using the custom analysis feature on DepMap.org, we performed a two-class comparison of Expression Public 22Q4 data with our addictive cell lines (COLO679, SKMEL5 and SKMEL28) as our 'in' group and our non-addictive cell lines (A375, HS294T and WM793) as our 'out' group. The resulting data are found in the supplementary materials. We performed GSEA[52] on these data using melanocytic, neural-crest-like and undifferentiated gene signatures that were previously defined[12] and can also be found in the supplementary materials.

Melanocytic or dedifferentiated melanoma classification. We performed ssGSEA on all 63 *BRAF*- and *NRAS*-mutant melanoma cell lines annotated in the DepMap Expression Public 22Q4 database with the melanocytic gene signature using the GenePattern platform[52–54].

MAPK-mutant melanoma with an enrichment score (ES) >2,500 was classified as melanocytic. All MAPK-mutant cell lines with an ES <2,500 were classified as dedifferentiated. The ESs for each cell line are in the supplementary materials. We used these classifications to compare *DUSP4* and *PPP6C* dependency scores and JunB protein levels via the DepMap custom analyses feature.

Definition of JunB transcriptional signature. We selected the top 100 upregulated genes from a JunB overexpression experiment in melanoma[44], found in the supplementary materials. Using this signature, we assigned every available cell line in DepMap an ES using ssGSEA. We correlated this score with the JunB expression to validate the signature. Following validation, we compared the ES of melanocytic and dedifferentiation melanoma. Both analyses were performed in the DepMap custom analyses feature.

Growth rate calculation

To calculate growth rates, cell populations were used at low passage numbers with measured drug resistance. Cells were plated in triplicate in 10 cm plates at 3,000 cells per plate in standard growth medium. The following day, cells were treated with drug or DMSO. After 6 days, the cells were lifted with 0.25% trypsin (Life Technologies) and counted using a Z2 Coulter Particle Count and Size Analyzer (Beckman Coulter). Effective growth rates (μ) were calculated from the number of cells plated (N_0) and the number counted (N) according to the equation:

$$\ln N = \ln N_0 + \mu\tau$$

where τ is the elapsed time (168 h).

Drug scheduling assay

After measuring growth rates, we plated cells in 15 cm plates with growth medium and no drug. The following day, we added the drug (or not) based on the indicated drug schedule. Cells were counted at the end of each completed schedule and replated as indicated. All drug schedules were established based on the interval between counts. For example, if cells were treated with 75% drug and counted every 4 days, they would be treated with the drug for 3 days and diluent for 1 day, counted and replated for the duration of the experiment. If a portion of the cells was discarded before replating, growth rates (μ) were calculated over the period from the number of cells plated at the beginning of the period (N_0) and the number counted at the end of the period (N) according to the equation above. These growth rates were then used to predict the total cell number as if no cells had been discarded. After the initial plating, which was always diluent only, the cells were replated into treatment determined by their schedule.

Statistics

All results are shown as means ± s.d. To compare groups, unless noted otherwise, P values were determined using unpaired, two-tailed Student's t-tests.

'Blind' adaptive therapy algorithm

We started by administering drug for some time ΔT and estimating the growth rate during that period. This period is followed by removing the drug for the same ΔT, and the drug-free (or 'holiday') growth rate is estimated. We then administered the condition (drug or no drug) corresponding to the lower growth rate and recorded the growth rate for each ΔT that passes. If the growth rate for the most recent ΔT surpasses that of the opposite condition, we switched the treatment condition for the next time window. We repeated this process for the remainder of the treatment time, recording new values for the population growth in drug and during treatment holidays and switching between treatments as they become optimal.

Spatial ABM

We use a 2D, on-lattice ABM using the Hybrid Automata Library[55]. The cells can be divided into sensitive and resistant populations and do not allow for mutation between cell types. All simulations are performed with a 200 × 200 lattice size with no flux boundary conditions. Cells are assumed to be randomly distributed to start. Sensitive and resistant cells attempt to divide at a constant rate determined by their environment (drug on or off). If at least one site in the cell's neighbourhood is empty, then the cell will divide and a daughter will now occupy the empty site. The neighbourhood size is assumed to be von Neumann (cells not impacted by the boundary have four neighbours). Cells die at a constant rate, which we assume (for simplicity) is equal for sensitive and resistant cells. Cell movement and migration are not allowed, and the drug environment is assumed to be homogenous. Dead cells are immediately removed from the lattice.

Reporting summary

Further information on research design is available in the Nature Portfolio Reporting Summary linked to this article.

Data availability

All data generated or analysed during this study are included in this published article (and its supplementary information files). Source data are provided with this paper.

Code availability

All code used in this study will be available on GitHub.

References

1. Larkin, J. et al. Five-year survival with combined nivolumab and ipilimumab in advanced melanoma. *N. Engl. J. Med.* **381**, 1535–1546 (2019).
2. Kreft, S. et al. MAPKinase inhibition after failure of immune checkpoint blockade in patients with advanced melanoma—an evaluation of the multicenter prospective skin cancer registry ADOREG. *Eur. J. Cancer* **167**, 32–41 (2022).
3. Atkins, M. B. et al. Combination dabrafenib and trametinib versus combination nivolumab and ipilimumab for patients with advanced *BRAF*-mutant melanoma: the DREAMseq Trial—ECOG-ACRIN EA6134. *J. Clin. Oncol.* **41**, 186–197 (2023).
4. Welsh, S. J., Rizos, H., Scolyer, R. A. & Long, G. V. Resistance to combination *BRAF* and MEK inhibition in metastatic melanoma: where to next? *Eur. J. Cancer* **62**, 76–85 (2016).
5. Das Thakur, M. et al. Modelling vemurafenib resistance in melanoma reveals a strategy to forestall drug resistance. *Nature* **494**, 251–255 (2013).
6. Sun, C. et al. Reversible and adaptive resistance to *BRAF*(V600E) inhibition in melanoma. *Nature* **508**, 118–122 (2014).
7. Hong, A. et al. Exploiting drug addiction mechanisms to select against MAPKi-resistant melanoma. *Cancer Discov.* **8**, 74–93 (2018).
8. Moriceau, G. et al. Tunable-combinatorial mechanisms of acquired resistance limit the efficacy of *BRAF*/MEK cotargeting but result in melanoma drug addiction. *Cancer Cell* **27**, 240–256 (2015).
9. Kong, X. et al. Cancer drug addiction is relayed by an ERK2-dependent phenotype switch. *Nature* **550**, 270–274 (2017).
10. Algazi, A. P. et al. Continuous versus intermittent *BRAF* and MEK inhibition in patients with *BRAF*-mutated melanoma: a randomized phase 2 trial. *Nat. Med.* **26**, 1564–1568 (2020).
11. Arozarena, I. & Wellbrock, C. Phenotype plasticity as enabler of melanoma progression and therapy resistance. *Nat. Rev. Cancer* **19**, 377–391 (2019).
12. Tsoi, J. et al. Multi-stage differentiation defines melanoma subtypes with differential vulnerability to drug-induced iron-dependent oxidative stress. *Cancer Cell* **33**, 890–904.e5 (2018).

13. Landsberg, J. et al. Melanomas resist T-cell therapy through inflammation-induced reversible dedifferentiation. *Nature* **490**, 412–416 (2012).
14. Mehta, A. et al. Immunotherapy resistance by inflammation-induced dedifferentiation. *Cancer Discov.* **8**, 935–943 (2018).
15. Kim, Y. J. et al. Melanoma dedifferentiation induced by IFN-γ epigenetic remodeling in response to anti-PD-1 therapy. *J. Clin. Invest.* **131**, e145859 (2021).
16. Müller, J. et al. Low MITF/AXL ratio predicts early resistance to multiple targeted drugs in melanoma. *Nat. Commun.* **5**, 5712 (2014).
17. Konieczkowski, D. J. et al. A melanoma cell state distinction influences sensitivity to MAPK pathway inhibitors. *Cancer Discov.* **4**, 816–827 (2014).
18. Johannessen, C. M. et al. A melanocyte lineage program confers resistance to MAP kinase pathway inhibition. *Nature* **504**, 138–142 (2013).
19. Enriquez-Navas, P. M. et al. Exploiting evolutionary principles to prolong tumor control in preclinical models of breast cancer. *Sci. Transl. Med.* **8**, 327ra24 (2016).
20. Silva, A. S. et al. Evolutionary approaches to prolong progression-free survival in breast cancer. *Cancer Res.* **72**, 6362–6370 (2012).
21. Gatenby, R. A., Silva, A. S., Gillies, R. J. & Frieden, B. R. Adaptive therapy. *Cancer Res.* **69**, 4894–4903 (2009).
22. Smalley, I. et al. Leveraging transcriptional dynamics to improve *BRAF* inhibitor responses in melanoma. *eBioMedicine* **48**, 178–190 (2019).
23. Lin, K. H. et al. Using antagonistic pleiotropy to design a chemotherapy-induced evolutionary trap to target drug resistance in cancer. *Nat. Genet.* **52**, 408–417 (2020).
24. Zhao, B. et al. Exploiting temporal collateral sensitivity in tumor clonal evolution. *Cell* **165**, 234–246 (2016).
25. Maltas, J. & Wood, K. B. Pervasive and diverse collateral sensitivity profiles inform optimal strategies to limit antibiotic resistance. *PLoS Biol* **17**, e3000515, https://doi.org/10.1371/journal.pbio.3000515 (2019).
26. Maltas, J., Krasnick, B. & Wood, K. B. Using selection by nonantibiotic stressors to sensitize bacteria to antibiotics. *Mol. Biol. Evol.* **37**, 1394–1406 (2020).
27. West, J., Ma, Y. & Newton, P. K. Capitalizing on competition: an evolutionary model of competitive release in metastatic castration resistant prostate cancer treatment. *J. Theor. Biol.* **455**, 249–260 (2018).
28. Wargo, A. R. et al. Competitive release and facilitation of drug-resistant parasites after therapeutic chemotherapy in a rodent malaria model. *Proc. Natl Acad. Sci. USA* **104**, 19914–19919, https://doi.org/10.1073/pnas.0707766104 (2007).
29. Kaznatcheev, A., Peacock, J., Basanta, D., Marusyk, A. & Scott, J. G. Fibroblasts and alectinib switch the evolutionary games played by non-small cell lung cancer. *Nat. Ecol. Evol.* **3**, 450–456 (2019).
30. Farrokhian N. et al. Measuring competitive exclusion in non-small cell lung cancer. Sci Adv. 8, eabm7212 (2022); https://science.org/doi/10.1126/sciadv.abm7212
31. Korolev, K. S., Xavier, J. B. & Gore, J. Turning ecology and evolution against cancer. *Nat. Rev. Cancer* **14**, 371–380 (2014).
32. Li, Y., Cheng, H. S., Chng, W. J. & Tergaonkar, V. Activation of mutant TERT promoter by RAS–ERK signaling is a key step in malignant progression of *BRAF*-mutant human melanomas. *Proc. Natl Acad. Sci. USA* **113**, 14402–14407 (2016).
33. Khaliq, M., Manikkam, M., Martinez, E. D. & Fallahi-Sichani, M. Epigenetic modulation reveals differentiation state specificity of oncogene addiction. *Nat. Commun.* **12**, 1536 (2021).
34. Tsherniak, A. et al. Defining a cancer dependency map. *Cell* **170**, 564–576.e16 (2017).
35. Luebker, S. A. & Koepsell, S. A. Diverse mechanisms of *BRAF* inhibitor resistance in melanoma identified in clinical and preclinical studies. *Front. Oncol.* **9**, 268 (2019).
36. Rizos, H. et al. *BRAF* inhibitor resistance mechanisms in metastatic melanoma: spectrum and clinical impact. *Clin. Cancer Res.* **20**, 1965–1977 (2014).
37. Ito, T. et al. Paralog knockout profiling identifies DUSP4 and DUSP6 as a digenic dependence in MAPK pathway-driven cancers. *Nat. Genet.* **53**, 1664–1672 (2021).
38. Gutierrez-Prat N. et al. DUSP4 protects BRAF- and NRAS-mutant melanoma from oncogene overdose through modulation of MITF. *Life Sci. Alliance* **5**, e202101235 (2022); https://www.life-science-alliance.org/content/5/9/e202101235
39. Cho, E., Lou, H. J., Kuruvilla, L., Calderwood, D. A. & Turk, B. E. PPP6C negatively regulates oncogenic ERK signaling through dephosphorylation of MEK. *Cell Rep.* **34**, 108928 (2021).
40. Ji, Z. et al. MITF modulates therapeutic resistance through EGFR signaling. *J. Invest. Dermatol.* **135**, 1863–1872 (2015).
41. Labrie, M., Brugge, J. S., Mills, G. B. & Zervantonakis, I. K. Therapy resistance: opportunities created by adaptive responses to targeted therapies in cancer. *Nat. Rev. Cancer* **22**, 323–339 (2022).
42. Shaffer, S. M. et al. Rare cell variability and drug-induced reprogramming as a mode of cancer drug resistance. *Nature* **546**, 431–435 (2017).
43. Su, Y. et al. Single-cell analysis resolves the cell state transition and signaling dynamics associated with melanoma drug-induced resistance. *Proc. Natl Acad. Sci. USA* **114**, 13679–13684 (2017).
44. Nyberg, W. A. et al. The bromodomain protein TRIM28 controls the balance between growth and invasiveness in melanoma. *EMBO Rep.* **24**, e54944 (2023).
45. Kavran, A. J. et al. Intermittent treatment of $BRAF^{V600E}$ melanoma cells delays resistance by adaptive resensitization to drug rechallenge. *Proc. Natl Acad. Sci. USA* **119**, e2113535119 (2022).
46. Strobl, M. A. R. et al. Spatial structure impacts adaptive therapy by shaping intra-tumoral competition. *Commun. Med.* **2**, 46 (2022).
47. Yu, H. A. et al. Phase 2 study of intermittent pulse dacomitinib in patients with advanced non-small cell lung cancers. *Lung Cancer* **112**, 195–199 (2017).
48. Killarney, S. T. et al. Executioner caspases restrict mitochondrial RNA-driven type I IFN induction during chemotherapy-induced apoptosis. *Nat. Commun.* **14**, 1399 (2023).
49. Martz, C. A. et al. Systematic identification of signaling pathways with potential to confer anticancer drug resistance. *Sci. Signal.* **7**, ra121 (2014).
50. Hart, T. et al. Evaluation and design of genome-wide CRISPR/SpCas9 knockout screens. *G3* **7**, 2719–2727 (2017).
51. Guzmán, C. et al. ColonyArea: an ImageJ plugin to automatically quantify colony formation in clonogenic assays. *PLoS One* **9**, e92444, https://doi.org/10.1371/journal.pone.0092444 (2014).
52. Subramanian, A. et al. Gene set enrichment analysis: a knowledge-based approach for interpreting genome-wide expression profiles. *Proc. Natl Acad. Sci. USA* **102**, 15545–15550 (2005).
53. Barbie, D. A. et al. Systematic RNA interference reveals that oncogenic KRAS-driven cancers require TBK1. *Nature* **462**, 108–112 (2009).
54. Reich, M. et al. GenePattern 2.0. *Nat. Genet.* **38**, 500–501 (2006).
55. Bravo, R. R. et al. Hybrid Automata Library: a flexible platform for hybrid modeling with real-time visualization. *PLoS Comput. Biol.* **16**, e1007635 (2020).

Acknowledgements

This study was supported by Duke University School of Medicine start-up funds and the Duke Cancer Institute (K.C.W.), and received grant support from an anonymous donor to the Duke Cancer Institute (K.C.W.), National Institutes of Health awards R01CA207083 and R01CA263593 (K.C.W.), NIH R35GM124875 (K.B.W) and the Duke Medical Scientist Training Program (T32 GM007171 to S.T.K.).

Author contributions

K.B.W and K.C.W. conceptualized the project. K.B.W., J.M., S.T.K., K.R.S. and K.C.W. were responsible for the methodology. Mechanistic and validation studies were performed by J.M., S.T.K., K.R.S., R.W. and M.A.R.S. Data were curated by J.M., S.T.K. and K.R.S. J.M., S.T.K. and K.R.S. were responsible for visualization. The original draft was written by K.B.W., J.M., K.R.S. and K.C.W. All authors reviewed and edited the paper. K.B.W. and K.C.W. supervised the project.

Competing interests

K.C.W. is a founder, consultant and equity holder at Tavros Therapeutics and Celldom and has performed consulting work for Guidepoint Global, Bantam Pharmaceuticals and Apple Tree Partners. All other authors declare no competing interests.

Additional information

Supplementary information The online version contains supplementary material available at https://doi.org/10.1038/s41559-023-02255-x.

Correspondence and requests for materials should be addressed to Kris C. Wood or Kevin B. Wood.

Peer review information *Nature Ecology & Evolution* thanks Andriy Marusyk and the other, anonymous, reviewer(s) for their contribution to the peer review of this work.

nature portfolio

Corresponding author(s): Kris C. Wood and Kevin B. Wood

Last updated by author(s): Oct 1, 2023

Reporting Summary

Nature Portfolio wishes to improve the reproducibility of the work that we publish. This form provides structure for consistency and transparency in reporting. For further information on Nature Portfolio policies, see our Editorial Policies and the Editorial Policy Checklist.

Statistics

For all statistical analyses, confirm that the following items are present in the figure legend, table legend, main text, or Methods section.

n/a	Confirmed	
☐	☒	The exact sample size (*n*) for each experimental group/condition, given as a discrete number and unit of measurement
☐	☒	A statement on whether measurements were taken from distinct samples or whether the same sample was measured repeatedly
☐	☒	The statistical test(s) used AND whether they are one- or two-sided *Only common tests should be described solely by name; describe more complex techniques in the Methods section.*
☒	☐	A description of all covariates tested
☐	☒	A description of any assumptions or corrections, such as tests of normality and adjustment for multiple comparisons
☐	☒	A full description of the statistical parameters including central tendency (e.g. means) or other basic estimates (e.g. regression coefficient) AND variation (e.g. standard deviation) or associated estimates of uncertainty (e.g. confidence intervals)
☐	☒	For null hypothesis testing, the test statistic (e.g. *F*, *t*, *r*) with confidence intervals, effect sizes, degrees of freedom and *P* value noted *Give P values as exact values whenever suitable.*
☒	☐	For Bayesian analysis, information on the choice of priors and Markov chain Monte Carlo settings
☒	☐	For hierarchical and complex designs, identification of the appropriate level for tests and full reporting of outcomes
☒	☐	Estimates of effect sizes (e.g. Cohen's *d*, Pearson's *r*), indicating how they were calculated

Our web collection on statistics for biologists contains articles on many of the points above.

Software and code

Policy information about availability of computer code

Data collection	-Cell Counting: Z2 Coulter Particle Count and Size Analyzer -Plate Reader for luminescence assays: TECAN infinite M1000Pro -Blot image scanning: Epson Perfection V600 Photo -DNA/RNA concentration measurement: Thermo Fisher NanoDrop Lite -FACS Analysis: Becton Dickinson FACSCanto II and Beckman Coulter Astrious Cell Sorter
Data analysis	-Statistical analysis and plotting were done in GraphPad Prism 8.0.2, 9.0.1 or Microsoft Excel 2016-2021 -Figures were prepared in Adobe Illustrator CC 2017, 2020 -Western blot and clonogenic plates images were scanned with EPSON Scan 3.9.4 -Clonogenic quanitfications were calculated in Imagej 1.51 -Flow cytometry data was analyzed in FlowJo (v10.9) -DepMap analyses were performed in the custom analyses data explorer portal (https://depmap.org/portal/interactive/) -

For manuscripts utilizing custom algorithms or software that are central to the research but not yet described in published literature, software must be made available to editors and reviewers. We strongly encourage code deposition in a community repository (e.g. GitHub). See the Nature Portfolio guidelines for submitting code & software for further information.

Data

Policy information about availability of data

All manuscripts must include a data availability statement. This statement should provide the following information, where applicable:

- Accession codes, unique identifiers, or web links for publicly available datasets
- A description of any restrictions on data availability
- For clinical datasets or third party data, please ensure that the statement adheres to our policy

All data generated or analyzed during this study are included in this published article (and its supplementary information files). All code used in this study will be available on GitHub.

Research involving human participants, their data, or biological material

Policy information about studies with human participants or human data. See also policy information about sex, gender (identity/presentation), and sexual orientation and race, ethnicity and racism.

Reporting on sex and gender	N/A
Reporting on race, ethnicity, or other socially relevant groupings	N/A
Population characteristics	N/A
Recruitment	N/A
Ethics oversight	N/A

Note that full information on the approval of the study protocol must also be provided in the manuscript.

Field-specific reporting

Please select the one below that is the best fit for your research. If you are not sure, read the appropriate sections before making your selection.

☒ Life sciences ☐ Behavioural & social sciences ☐ Ecological, evolutionary & environmental sciences

For a reference copy of the document with all sections, see nature.com/documents/nr-reporting-summary-flat.pdf

Life sciences study design

All studies must disclose on these points even when the disclosure is negative.

Sample size	As described, in vitro sample sizes ranged from n=3 to n=5 replicates per condition. Sample sizes were sufficient to identify significant changes as indicated in each figure.
Data exclusions	No data were excluded from analysis.
Replication	Experimental findings were performed at least 3 independent times. The experimental findings were reliably reproduced and all attempts were included in the presentation unless technical error prevented the completion of the experiment.
Randomization	No randomization was required for the in vitro cell line experimentation.
Blinding	No blinding of in vitro experiments was performed as each cell line requires different culture conditions.

Reporting for specific materials, systems and methods

We require information from authors about some types of materials, experimental systems and methods used in many studies. Here, indicate whether each material, system or method listed is relevant to your study. If you are not sure if a list item applies to your research, read the appropriate section before selecting a response.

Materials & experimental systems

n/a	Involved in the study
☐	☒ Antibodies
☐	☒ Eukaryotic cell lines
☒	☐ Palaeontology and archaeology
☒	☐ Animals and other organisms
☒	☐ Clinical data
☒	☐ Dual use research of concern
☒	☐ Plants

Methods

n/a	Involved in the study
☒	☐ ChIP-seq
☐	☒ Flow cytometry
☒	☐ MRI-based neuroimaging

Antibodies

Antibodies used	Primary antibodies were all purchased from Cell Signaling Technology and diluted at 1:1000. The catalog numbers are as follows: phospho-ERK (#9101), ERK (#4695), EGFR (#4267), PARP (#9542), vinculin (#4650), Beta-actin (#4970), AXL (#8661), p75NTR (#4201), MITF (#12590), SOX10 (#89356), SOX9 (#82630), JunB (#3753), p21 (#2947), HSP90 (#4874), FRA1 (#5281), and p-FRA1 (#3880).
Validation	Antibody validation of the manufacturers were available for all antibodies including positive and negative staining controls. Additionally we confirmed specificity of phospho-ERK (#9101), ERK (#4695), MITF (#12590), SOX10 (#89356), and JunB (#3753) antibodies through overexpression or knockout studies.

Eukaryotic cell lines

Policy information about cell lines and Sex and Gender in Research

Cell line source(s)	All cell lines were purchased from American Type Culture Collection (ATCC) or Duke University Cell Culture Facility (CCF). The commonly-used cancer cell lines used in this study were A375, SKMEL28, SKMEL5, UACC62, COLO679, WM793, and HS294T.
Authentication	All cell lines were authenticated prior to use using STR profiling.
Mycoplasma contamination	All cell lines were confirmed as mycoplasma-free upon receipt.
Commonly misidentified lines (See ICLAC register)	No cell lines were misclassified.

Flow Cytometry

Plots

Confirm that:

☒ The axis labels state the marker and fluorochrome used (e.g. CD4-FITC).

☒ The axis scales are clearly visible. Include numbers along axes only for bottom left plot of group (a 'group' is an analysis of identical markers).

☒ All plots are contour plots with outliers or pseudocolor plots.

☒ A numerical value for number of cells or percentage (with statistics) is provided.

Methodology

Sample preparation	Pelleted cells were resuspended in 100 µL of Flow Cytometry Staining Buffer (eBioscience™, #00-4222-26) at a concentration of 100,000 cells/ml. APC anti-human EGFR Antibody (Biolegend, #352906) or APC Mouse IgG1, κ Isotype Ctrl (FC) Antibody (Biolegend, #400122) was added at 2000x to the suspended cells, and the reaction was left to incubate at room temperature for 30 minutes. Cells were washed thrice with 1 ml of Flow Cytometry Staining Buffer. Data were acquired with a FACSCanto II (BD Biosciences) flow cytometer, and the results were analyzed in Flowjo (TreeStar).
Instrument	Becton Dickinson FACSCanto II
Software	FlowJo (v10.9)
Cell population abundance	Cell populations were entirely pure of any contaminants.
Gating strategy	Cells were gated for live cells based on FSC/SSC and singlets based on FSC.

☒ Tick this box to confirm that a figure exemplifying the gating strategy is provided in the Supplementary Information.